CrystEngComm

Accepted Manuscript

ROYAL SOCIETY OF CHEMISTRY

www.rsc.org/crystengcomm

CrystEngComm

ARTICLE

Core-Shell nano Crystallite Growth via Heterogeneous Interface Manipulation

Received 00th January 20xx,
Accepted 00th January 20xx

DOI: 10.1039/x0xx00000x

www.rsc.org/

Po-Wei Yang,[a] Yu-Ting Liu,[b] Shu-Ping Hsu,[c] Kuan-Wen Wang,[c] U-Ser Jeng,[d] Tsang-Lang Lin,[a] and Tsan-Yao Chen[*a,e]

The growth of platinum shell crystal at heterogeneous facets of ruthenium metal nanocrystal was investigated via *in-situ* small angle X-ray scattering analysis. Our results illustrated that the pathways of shell crystal growth are mainly dominated by controlling the incubation time prior to the thermal reduction of Pt ions by polyol radicals. For the cases with short incubation time, the shell crystal grow at radial facets and face facets of Nano-cylinder core tend to grow into <111> and <200> facets via heterogeneous nucleation and crystal growth with and without assisting by transmetallation, respectively. On the other hand, severe chemical etching was found prior to the shell crystal growth in the case with incubation for 2 hours. Consequently, the shell structure is developed by the nucleation of PtRu alloy followed by the growth of Pt crystal. In both cases, the dynamic restructure at core-shell interface was found upon deposition of the shell crystal. These results enable the development of core-shell crystallite in expected configurations with tuneable atomic structure.

Introduction

The control on structures of nanoscaled electrocatalysts (NCs) is one of the most crucial techniques for development of fuel cell system in high conversion efficiency and chemical stability. On heterogeneous catalysis principle, the development of NCs in different chemical identities and geometrical conformations is a general and effective way that meet these criteria[1, 2]. From these concepts, the deciding structure factors in the surface activities include the ratio of facets that exposing to particle surface[3], the heteroatomic alloying, and most importantly the near-surface lattice strain of NCs.[4-6]

The redox reactivity of bimetallic catalyst was optimized by the growing their structure in the form of alloyed nanoparticle,[7, 8] thin-films, artificial architecture (nano-tubes and flakes), and most importantly core-shell NCs (in the shape of spherical, disk, and even rod). Combining results of density functional theory (DFT) estimation[9, 10] and experimental spectra characterizations[11-13], the core-shell NCs had been proved to be the most effective, simplest, and programmable platform for electrocatalytic applications among these structures. To optimize the activity and stability of such NCs, one can manipulate the structure / constituents in their intra-particle components in the three regions including (1) the size, chemical identity, and shape of the core crystal[14, 15], (2) the type of heterojunction (e.g., metal – metal or metal – oxide) and extent of heteroatomic intermix at interface[2, 16], and (3) the thickness, identity, the core coverage, and surface oxidation of the shell crystal[10, 17]. These factors are strongly inter-correlated and complementary contributing to the surface redox activity of the NCs.

On these considerations, extensive works had been done on the structure evolution issues of shell and core crystal and their corresponding impacts on redox performance core-shell NCs including (1) the changes of shell crystal thickness[17], (2) the atomic relocation at core-shell interface upon growing the shell crystal[17, 18], (3) the identity and size of core crystal[14], and (4) the impacts of the above three structural parameters on the valence band structure[15, 19, 20]. These studies disclosed most issues of the surface reactivity for NCs on the static structure information. With proper understanding of the fundamental insides, these results likely draw a clear picture with strategies for developing the future Fuel Cell electrocatalysts. Unfortunately, there is a missing gap between the control of NCs configurations and the design of the NCs properties due to the lack of time resolved structural information in particular at the core-shell interface.

Here, we demonstrate that the thickness and atomic intermix of shell crystal (SC) atop core crystal (CC) are strongly dominated by the atomic ratios of SC/CC precursors, the atomic packing density of core crystal facets, and the pre-

[a] Department of Engineering and System Science, National Tsing Hua University, Hsinchu 30013, Taiwan Fax: +886 3 5728445; Tel: +886 3 5742671; E-mail: chencaeser@gmail.com.
[b] Department of Soil and Environmental Sciences, National Chung-Hsing University, Taichung, Taiwan. Yliu21@gmail.com
[c] Institute of Materials Science and Engineering, National Central University, Taoyuan 32001, Taiwan. kuanwen.wang@gmail.com
[d] National Synchrotron Radiation Research Center, Hsinchu 30076, Taiwan. usjeng@nsrrc.org.tw
[e] Institute of Nuclear Engineering and Science, Hsinchu 30013, Taiwan Fax: +886 3 5728445; Tel: +886 3 5742671; E-mail: chencaeser@gmail.com
Electronic Supplementary Information (ESI) available: [details of any supplementary information available should be included here]. See DOI: 10.1039/x0xx00000x

incubation time upon crystal growth. For the case without pre-incubation treatment, the shell crystal grown following the behaviours of heterogeneous nucleation and crystal growth mechanism resulting the (island and film coexist geometry). On the other hand, for the case with pre-incubation treatment, the core crystal surface was exposed to the system containing high concentration of electronegative metal ions for 2 hours. In this circumstance, the shell crystal is developed by the nucleation of PtRu alloy followed by the growth of Pt crystal. To the best of our knowledge, this study is the very first demonstration on monitoring the dynamic atomic restructure of NCs at core-shell interface upon deposition of the shell crystal by combining the *in-situ* small angle and wide angle X-ray scattering (S/WXAS) at a spatial resolution of sub-atomic scale.

Experimental Section

The shell crystal growth mechanisms of the experimental NCs were complimentary investigated by *in-situ* small angle X-ray scattering (SAXS). The corresponding shell heteroatomic intermixes were determined by *in-situ* wide angle X-ray scattering (WXAS). The impacts of heteroatomic intermix on the shell crystal growth was revealed by changing the pre-incubation (immersing) time of Ru core or the shell metal ion concentrations in the reaction system.

Synthesis of ruthenium Core NPs

The ruthenium core NPs (Ru NPs) were synthesized in a concentration of 100 mM ruthenium chloride ($RuCl_3 \cdot xH_2O$, 99.5%) in ethylene glycol (EG, 99.5%). In the reaction system, the concentration of stabilizer (polyvinylpyrrolidone PVP-40, MW ~42,000, 99%) was set to 10wt%. The reaction was conducted at 160°C for 2 h. After that, the product was cooled to room temperature for the subsequent *in-situ* experiments.

***In-situ* SAXS/WAXS characterizations**

The SAXS/WAXS experiments were conducted at beamlines of BL-23A1 in National Synchrotron Radiation Center (NSRRC, Taiwan) and at Taiwan beamline of BL-12B2 in Spring-8 (Koto, Japan). To gain the proper detection dimension (from 0.008 $Å^{-1}$ to 0.6 $Å^{-1}$), the incident X-ray wavelength was selected to be 0.82667 Å (15.0 keV) and the sample to detector distance was set to be 2427.6 mm[21]. For conducting the *in-situ* experiments, a heating sample cell (sample thickness = 2.7 mm) containing two X-ray transmittable window (mica foil, 20 μm thick) and temperature programmable stage was employed. The SAXS and WAXS signals were collected by Pilatus 1M-F area detector (7 ms/frame, 169 mm by 179 mm) and Mythen-3k linear detector (2.5 ms/frame, 8mm by 18 mm), respectively. To reveal the effects of shell precursor ($H_2PtCl_6 \cdot 6H_2O$, 99 at%) concentration to the shell crystal growth mode, two CS/CC precursor ratios (1.0 and 2.0) were selected for growing the core-shell NCs and the corresponding time resolved structure parameters were compared. The effects of interface heteroatomic intermix on the shell crystal growth were conducted by immersing the Ru core crystal in the EG solution containing a Pt/Ru ratio of 3.0 for 2 hours prior to the *in-situ* SAXS and WAXS experiments. To determine the preference of shell crystal growth at different core facets, the WAXS signal was collected simultaneously with that of SAXS. The entire experiment was conducted under ambient atmospheric conditions. Upon the in-situ experiments, the temperature of reaction cell were controlled by a remote-controller with a thermal history of 3.1°C min^{-1} in the ramp up region (30 to 140°C) and then kept at 140°C for 2 h. The thermal profile is shown by the dashed line in green in **Fig. 2a**, **2b**, and **2c**.

SAXS model analysis

The structure parameters of experimental core-shell NCs were derived by fitting the corresponding SAXS spectra with a scattering function comprising models of fractal cylinder aggregates[22-24] and poly core-shell cylinder[25, 26]. In this function, considering the momentum transfer of incident X-ray photons that encountering the diffused surface of fractal aggregate, the outmost facets, and interface in core–shell cylinder particles with polydispersion in core size; the SAXS spectra intensity can be expressed by the combination of the contributions for scattering X-rays from the inter-particle fractal model ($Q < 0.007$ $Å^{-1}$) and the intra-particle core–shell cylinder particle ($Q > 0.007$ $Å^{-1}$). The numerical expression is shown in Equation (1):

$$I(Q) = A^{FC} \cdot P(Q)^{FC} \cdot S(Q)^{FC} + A^{PCSC} \cdot P(Q)^{PCSC} \cdot S(Q)^{PCSC} \quad (1)$$

where, A is the number density of the aggregates and particles. The structure factor $S(Q)$ and the particle form factor $P(Q)$ both are the function of momentum transfer Q ($Q = (4\pi / \lambda) \times \sin(\theta)$, where θ denotes the angle between the incident and the scattered beams at a wavelength of λ). Symbols of *FC* (fractal cylinder) and *PCSC* (poly core–shell cylinder) on the superscript identify which model the parameter belongs to. The function "$P(Q)^{FC}$ and $P(Q)^{PCSC}$ are the scattering X-rays from randomly distributed cylinder "building block" particles in fractal aggregate and in the core-shell cylinder particle, respectively. These cylinder particle having the average and core radius of R_P and R_C, the core length of H_C, the polydispersity of the core dimension (P), the shell thickness at radius (T_R) and face (T_F) facets, the volume fraction ϕ, and scattering length density (SLD) difference from the solvent (i.e., $\Delta\rho_P = \rho_P - \rho_{solv}$, $\Delta\rho_{core} = \rho_C - \rho_{solv}$ and $\Delta\rho_{shell} = \rho_S - \rho_{solv}$; where ρ_P is the average SLD of individual scattering object in the fractal aggregate and is determined by the ratio of core/shell precursor ratios)[24].

Results and Discussions

Nano structure evolutions of core-shell NCs

CrystEngComm

ARTICLE

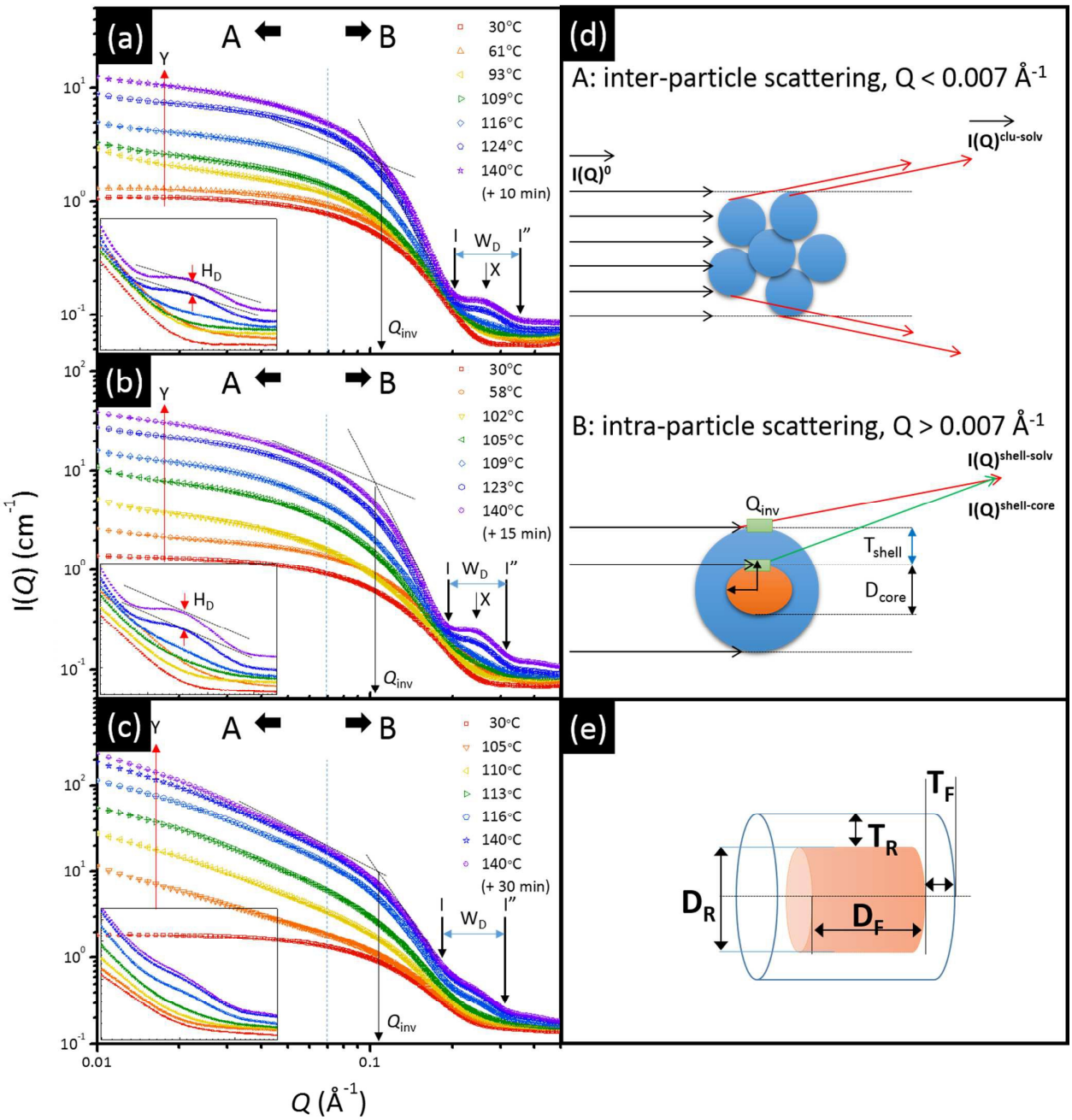

Fig. 1 *In-situ* SAXS spectra of Rucore-Ptshell NPs without ((**a**) Pt/Ru = 1.0 at% and (**b**) Pt/Ru = 2.0 at%) and with pre growth transmetallation incubation reaction ((**1c**) Pt/Ru = 3.0 at%). (**d**) the models of intraparticle scattering from randomly ordered "oblate" and "core-shell oblate" nanoparticles discussed, and (e) the scheme for the model for SAXS fitting analysis; where T_F refer to thickness of face shell, T_R refer to thickness of radial shell, D_F refer to diameter of core crystal at face facet, and D_R refer to diameter of core crystal at radial facet.

CrystEngComm

ARTICLE

The *in-situ* SAXS spectra [I(*Q*) vs *Q*] of the core-shell NCs in the SC/SS atomic ratios of 1.0, 2.0, and 3.0 are shown in **Fig. 1a**, **1b**, and **1c**, respectively. The corresponding scheme for the X-ray scattering interference pathways and the model for fitting the SAXS spectra are shown in **Fig. 1d** and **1e**, respectively. For NCs with Pt/Ru = 1.0, as indicated in **Fig. 1a** and **1d**, there are five features including arrow Y in the low *Q* region (region A, which correlating to the size of scattering matters: diameter of particle and the aggregate of particles), the inversion point of the spectrum (arrow Q_{inv}), and the centre (arrow X) with the width (W_D) / height (H_D) of the first scattering hump (between I and I") in the high *Q* region (region B) are found in the SAXS spectrum. These features are affected by the geometric parameters of the polymer blended NCs. In region A, the intensity at the near *Q* zero range (I_0) is caused by the contribution of incident X-ray at low contact angles to the scattering substances (i.e., the fractal clusters of NCs in our case). Given that the experiments were conduct in dilute systems (where the metal contents were set less than 40 mM), from colloidal scattering theory, the increasing I_0 can mainly attributed to the increasing of cluster size ξ (I_0 α ξ^6) and slightly the packing density (fractal dimension) of the NCs in the fractal cluster / aggregate. Here, three different stages were found upon increasing temperature in the system: (1) A slight increase of intensity was found simultaneously at regions A (inter-particle interferences) and B (intra-particle interferences). It suggests the increasing surface defects at the core crystal surface that both contributing to the scattering intensity in the entire spectrum. Given that the number density of scattering substances (Ru core NCs) remain unchanged, such phenomenon can be attributed to the mild atomic relocation at the Ru crystal surface due to a transmetallation between Pt^{4+} ion and Ru metal atoms (Ru^0) from room temperature to 61°C. The I_0 is increased by 10-folds with temperature till 138°C. It could be the results of increasing NCs size (D_{NCs}) upon growing the shell crystal and consequently the size expansion of the cluster (ξ). At 140°C, the I_0 increased with reaction time and can be attributed to the deposition of residual Pt^{4+} and Ru^{3+} ions at the NCs. A intersection point for the tangential lines of linear regions at the A and B regions is found on the SAXS spectrum. It's position (Q_{inv}) is a function of the curvature factors at outmost surface of scattering substance (NCs). Above the Q_{inv} (~0.11 $Å^{-1}$), the X-ray scattering intensity rapidly decreased with increasing momentum transfer (*Q*). From typical scattering theory, this feature coincides to the presence of out of phase scattering waves between the centre of incident beam and the first order scattering maximum (denoted by arrow X) at the SAXS spectrum; where Q_{inv} and Q_X are reversely proportional to the size (or the aspect ratio of longitude and latitude axes) and the shell crystal thickness (T_{shell}) of the NCs, respectively. The scattering hump (denoted by arrows I and I") is originated from the interferences of X-ray waveforms at the intra-particle boundaries (i.e., scattering within core crystal body and between the core-shell interface and the outmost surface of NCs). Here, H_D and W_D are inversely proportional to the roughness of core-shell (shell-solvent) interfaces and the polydispersity (η) of core diameter (D_{core}) and T_{shell}, respectively. For NCs with Pt/Ru = 2.0 (see **Fig. 1b**), the higher increasing rate of $I(Q)_Y$ from room temperature to 58°C indicates that the larger extent of Pt^{4+} ion to Ru^0 replacement compared to that of Pt/Ru = 1.0. The downshift of Q_{inv} is a direct indication for the reducing of NCs curvature at outmost surface and aspect ratio of scattering substances due to increasing T_{shell} and the uneven "chemical etching by transmetallation replacement" at longitude and latitude facets on Ru core. In addition, the narrowing W_D together with enhancing H_D correspond to the reducing of η for D_{core} (T_{shell}) and roughness for interfaces of shell crystal (at outmost surface and core-shell interface).

The transmetallation effects on the shell crystal growth are elucidated at the NCs with Pt/Ru = 3.0. In this case, the Ru NCs was interacted with Pt^{4+} ions in the reaction solution at room temperature for 2h (pre-growth transmetallation incubation time) prior to the thermal reduction. As shown in **Fig. 1c**, the I_0 of Pt/Ru = 3.0 is decreased by ~10% compared to that of Pt/Ru = 1.0 NCs at room temperature. It corresponds to the shrinkage of core size by 3 – 5% due to the certain extent of Ru dissolution (in particularly the etching / removal of surface adatoms) by transmetallation pathways during the pre-thermal reduction process. By increasing temperature till 140°C, the I_0 is increased by more than 2 orders (from 1.1 to -folds). This feature can be explained by the increasing of scattering length density (SLD) and crystal dimension (particle size, D_{avg}) upon growing high SLD Pt ($1.32*10^{-4}$ $Å^{-2}$) shell atop the low SLD Ru core surface ($9.22*10^{-5}$ $Å^{-2}$). By keeping reaction temperature (T^r) for 1.5h, the I_0 is doubled and can be attributed to mainly the increasing number density (due to the solvent evaporation) of NCs. Meanwhile, the intensity decay rate ($\Delta I(Q)/\Delta Q$) in region A is determined to be ~3900 (cm^{-1} * $Å^{-1}$) and is found one order higher than that of Pt/Ru =1.0 (~250) and 2.0 (~700). Such dramatic intensity decay illustrates the complexity of X-ray inferences between waveforms that outgoing from Pt shell and Ru core regions due to the formation of a thin layer Pt/Ru alloy (which slightly attenuate the intensity and randomize the phase contrast of scattering X-ray waveforms) at core-shell interface prior to the growth of Pt shell crystal on Pt/Ru = 3.0 NCs. This phenomenon is further

revealed by the upshift of Q_{inv} (reducing of shell thickness) and the broadening of scattering hump (reducing of H_D/W_D ratio) at the region B.

Growth mode of shell crystal

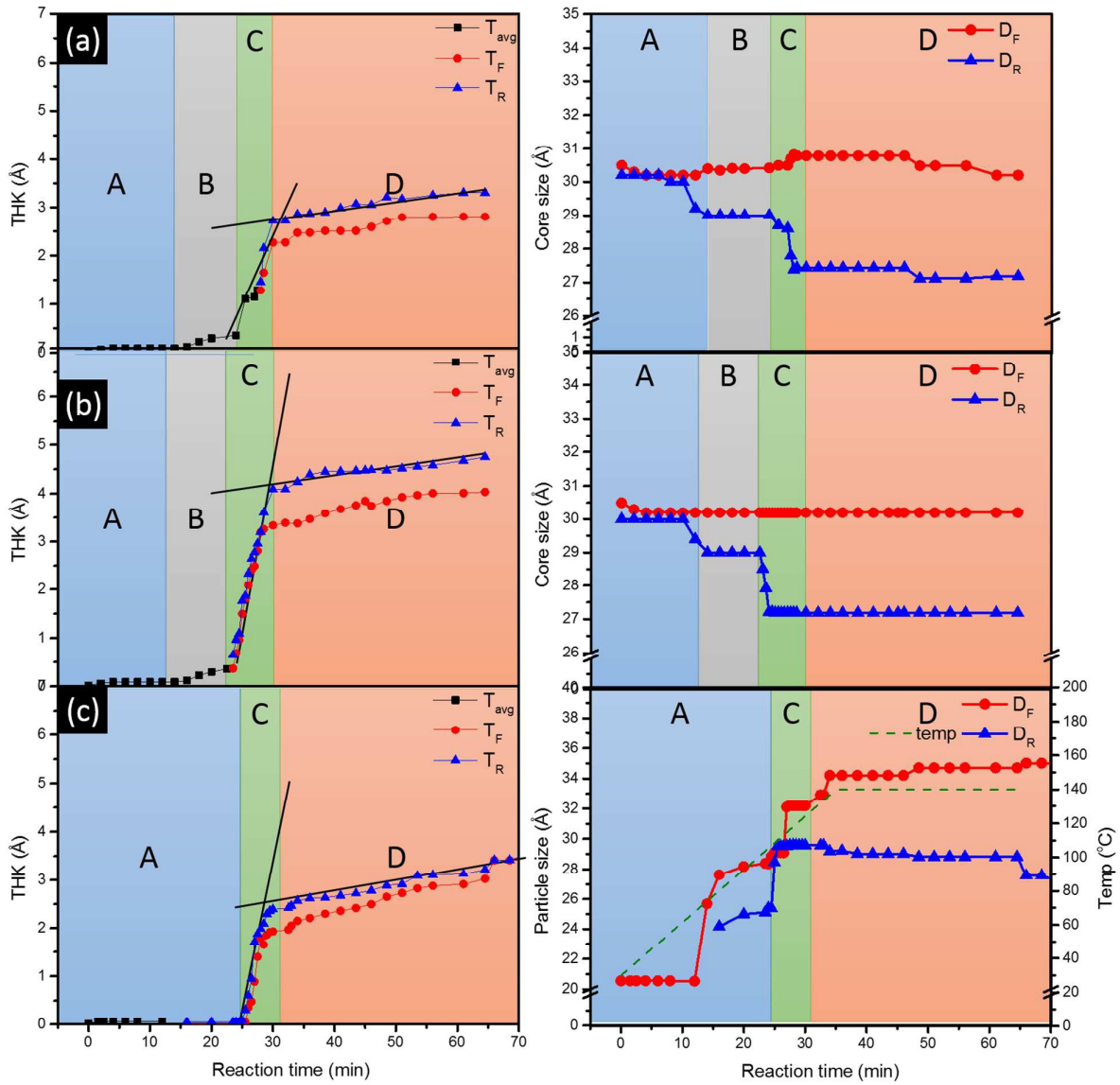

Fig. 2 SAXS determined shell crystal thickness (left side) and core diameter (eight side) for the Rucore-Ptshell NPs with reaction time in a ratios of (a) Pt/Ru = 1, (b) Pt/Ru = 2, (c) Pt/Ru = 3. (the corresponding polydispersity of the three NPs during in-situ crystal growth are shown in Fig. S1). The regions A, B, C, and D correspond to the transmetalation incubation, nucleation, shell crystal growth, and surface restructure, respectively, during the liquid state epitaxy shell crystal growth at the heterogeneous core surface. (d) the scheme for the scattering model of core-shell NPs. The parameters T_{avg}, T_F, T_R, D_F, and D_R denote the thickness of shell crystal in average, at face facet, at radial facets, the diameter of core crystal at face facet, and the diameter of core crystal at radial facet, respectively.

After investigating the effects of Pt precursor concentration and transmetallation incubation time on steric configurations of shell components, the corresponding impacts on the growth mode of shell crystal were revealed by using the quantitative structural parameters of core-shell NCs as changes with reaction time basing on the heterogeneous nucleation – growth theory and the chemical reaction kinetics. For this derivation, the intra-particle structure parameters of the core-shell NCs were determined by fitting the SAXS spectra with the scattering model of Equation (1). The obtained shell crystal thickness (T_F at face facets, T_R at radial facets, and T_{avg} the average shell crystal thickness) of Pt/Ru = 1.0, 2.0, 3.0 NCs as a function of reaction time and temperature were shown in **Fig. 2a**, **2b**, and **2c**, respectively, and the corresponding core crystal size for these NCs were shown in the right hand side. From the results of model analysis we can notice that the shape of experimental NCs is determined to be nano-disk (described in ESI).

For Pt/Ru = 1.0 NCs (**Fig. 2a**), the growth rate of shell crystal thickness ($\Delta T_j/\Delta t$, $_j$ denotes $_F$, $_R$, and $_{avg}$) can be divided into four regions; where regions A, B, C, and D corresponding to the reaction times taken by transmetallation incubation (surface flattening by removing Ru adatoms), nucleation, crystal growth, and surface restructure, respectively, upon growing shell crystal atop core crystal surface. In region A, only the T_{avg} is denoted at the temperature below 125°C. This is because the incomplete coverage on both face and radial facets at core surface and thus the indistinct $\Delta T_F/\Delta t$ and $\Delta T_R/\Delta t$. It is important to note a decrease of D_R by ~2.2Å (~0.9 to 1.0 atomic layer thick) coinciding to the preferential transmetallation at radial facets from 60 to 80°C. Further increasing temperature to 105°C (region B) slightly grow the T_{avg} by 0.5Å indicating the nucleation of subatomic Pt clusters atop the opened facets of Ru core crystal. By increasing temperature higher than 105 till 140°C (region C), the T_R and T_F are increased by 2.4 and 1.9Å, respectively, corresponding to the $\Delta T_R/\Delta t$ and $\Delta T_F/\Delta t$ of 65.6 and 52.8 (nm * 10^3 * s^{-1}). In this region, the higher growth rate implies the lower activation energy (higher surface free energy) for the adsorption and subsequent reduction of Pt^{4+} ions at the radial facets comparing to that at the face facets. In region D, the reaction was kept at 140°C. The subsequent ΔT_R and ΔT_F are determined to be the same value of ~0.6Å and consequently resulting in the $\Delta T_R/\Delta t$ and $\Delta T_F/\Delta t$ of 2.8 and 2.6 (nm * 10^3 * s^{-1}), respectively. The growth of shell crystal in such mild extent simultaneously with the reduction of diameter of crystal at radial facet (D_R) by 1.7Å can be considered the indications for the reduction of residual Pt^{4+} / Ru^{3+} ions and the restructure of the adatoms at the shell crystal surface (as well as core-shell interface) that in both ways minimizing the surface free energy of core-shell NCs. Taking these features together, the trajectory of shell crystal thickness with respect to the T^r coincide to the typical form of diffusion controlled heterogeneous nucleation and crystal growth pathways.

For Pt/Ru 2.0 NCs (see **Fig. 2b**), the nucleation temperature is reduced by 8°C (at 72°C) compared to that of NCs with Pt/Ru = 1.0. This phenomenon can be attributed to the pile-up effects of high density Pt^{4+} ions that stacking at the Ru core surface. It reduces the diffusion barrier high between the solvent and solid phases for the adsorption of Pt^{4+} ions and consequently enabling the nucleation of Pt clusters at reduced temperature. In this case, the $\Delta T_R/\Delta t$ and $\Delta T_F/\Delta t$ are facilitated by ~15% to 76.4 and 64.3 (nm * 10^3 * s^{-1}) in region C compare to that of Pt/Ru = 1.0 NCs. When increasing Pt/Ru to 3.0 and immersing the Ru core in Pt^{4+} solution for 2h (see **Fig. 2c**), the growth of pure Pt shell crystal was postpone to 112°C in region A and no nucleation step (region B) is found. The diameter of crystal at face facet D_F and D_R are determined to be 20.1 and 24.0Å, respectively. Both the two values are smaller than that of Pt/Ru = 1.0 and 2.0 indicating the presence of Ru dissolution via Pt^{4+} to Ru^0 replacement. In this case, the growth rate at T_R and T_F is determined to be 94.7 and 84.6 (nm * 10^3 * s^{-1}) which is the highest value among the three NCs. At Ru core facets, the shell crystal is grown by reducing the Pt^{4+} and Ru^{3+} ions by CHO: radicals at the surface facets of Ru core crystallite. The reaction can be described by "$aPt^{4+R}_{(l)}$ + $bRu^{3+D}_{(l)}$ + $cCHO:_{(l)}$ + $dRu_{(h,k,l)(S)}$ ←→ $eRu^0_xPt^0_{1-x}@Ru_{(h,k,l)(S)}$"; where Pt^{4+_R}, Ru^{3+_D}, and $Ru_{(h,k,l)S}$ denote the residual Pt^{4+} and dissolved Ru^{3+} ions after nucleation reaction, and the molar volume of the solid material (i.e., number density of reaction sites (area) at (h,k,l) facets of Ru crystallites). Considering to the concentration of reagents, the shell crystal growth rate (R_{rate}) shall linearly proportional to the ideal chemical reaction kinetics with an approximation of Equation (2):

$$R_{rate} = \xi \times k \frac{[Pt^{4+R}]^a [Ru^{3+D}]^b [CHO:]^c [Ru_{(hkl)(S)}]^d}{[Ru_x^0 Pt_{1-x}^0 @ Ru_{(hkl)(S)}]^e} \quad (2)$$

where ξ is the surface free energy dependent crystal growth rate at a singular facet dominating by the diffusion kinetics of atoms at solid surface.[16, 27, 28] Since the CHO: radical is decomposed from solvent molecules and the number density of solid phases (i.e., concentrations of core crystallites "$Ru_{(h,k,l)(S)}$" in our case) remain unchanged, these values can be set as constant that without affecting the reaction kinetics. When comparing the crystal growth rate at the same facets of NCs in difference Pt/Ru ratios, the effects of surface free energy can be normalized to the same value. For Pt/Ru = 2.0 NCs, the Ru^0 → Ru^{3+} dissolution rate is far slower than that of thermal reduction of Pt^{4+} (i.e., $[Pt^{4+R}] >> [Ru^{3+D}]$). Hence, the R_{rate} is dominated by the concentration of Pt^{4+} in a reaction order of b = ~1.7. The R_{rate} of Pt/Ru = 3.0 NCs is ~45% higher than that of Pt/Ru = 1.0 NCs and corresponds to the reaction order of b = ~1.3. Such low order reaction indicates the reduced correlation of $[Pt^{4+R}]$ to the R_{rate} and again consistently rationalizing the competitions between Ru^{3+D} and Pt^{4+R} reduction at Ru core surfaces (i.e., the formation of PtRu alloy layer in region C prior to the growth of pure Pt shell in region D). With increasing reaction time to 25 mins, the D_R and D_F were increased to 29.1 Å in region A. Given that no shell crystal growth was found, this structure evolution is regarded as the core crystal regrowth and can be rationalized by the minimization of total surface free energy with increasing the stacking layers of high surface free energy facets of Ru crystallite. The uneven regrowth was found on D_F and D_R in the subsequent reaction regions (C and D). At radial facets, the D_R reaches the saturation size suggesting the equilibrium of thermal reduction of Ru^{3+} by CHO: radicals. On the other hand, the D_F are further increased to ~34 Å indicating that the residual Ru^{3+} tend to grow at the face facets. Such selective regrowth seems controversial, however, can be rationalized consider to the thermodynamics equilibrium of chemical reduction reactions at crystal facets with different surface energies as consistently revealed in the subsequent wide angle X-ray scattering (WAXS) results (**Fig. 3**). These proposed mechanisms on shell crystal growth are consistently illustrated by the changes of polydispersity of core diameter with the reaction time.

Orientation identification of shell crystal growth

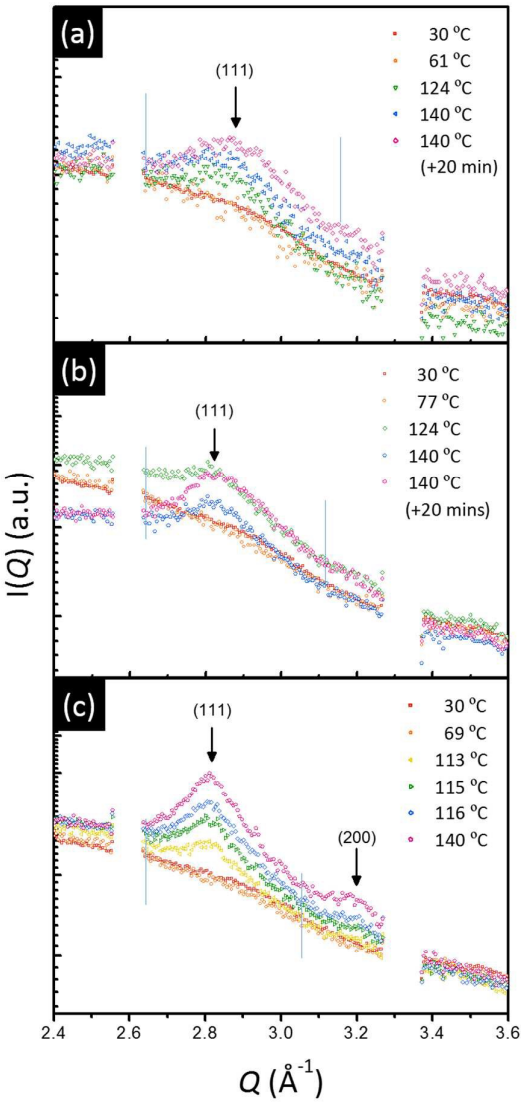

Fig. 3 WAXS spectra and corresponding average crystal size of Rucore-Ptshell NPs in atomic ratios of (a) Pt/Ru = 1, (b) Pt/Ru = 2, and (c) Pt/Ru = 3 during in-situ crystal growth. (d) the corresponding changes of lattice space for the experiment NCs with reaction time.

The orientations of the shell crystal facets are determined by using *in-situ* wide angle X-ray scattering (WAXS) analysis. The obtained WAXS spectra of the Pt/Ru = 1.0 (2.0) and 3.0 NCs are shown in **Fig. 3a**, **3b**, and **3c**, respectively, where the corresponding changes of lattice space are compared in **Fig. 3d**. For Pt/Ru = 1.0 NCs, the presence of diffraction line of (111) facet at Q = 2.88Å^{-1} indicating the formation of sufficient volume of scattering bulk with long-range ordering by the transmetallation induced atomic restructure at T^r > 124°C.[3, 29, 30] Accordingly, the lattice space is determined to be 2.213Å which is 2.3% compressed comparing to that of Pt (111) facet (2.265Å). It implies the assembly of Pt^0 atom in pseudo alloy cluster by the confinement of Ru {1010} facets ($d_{\{1010\}}$ = 2.18Å). The $d_{(111)}$ is further compressed to 2.195Å with increasing reaction time to 55 mins at T^r = 140°C. This value corresponds to the extent of Ru alloying in Pt by ~82 at% (according to Vagard's law), however, disobey the thermodynamic nature of homoatomic arrangement tendency of Pt crystal.[3] Therefore, such dramatic lattice space difference could only be rationalized by the combination effects of near surface alloying[31] and the compression of Pt crystal by adjacent to Ru facets (~3.1%)[5]. For Pt/Ru = 2.0 NCs (spectra were shown in **Fig. 3b**), the (111) diffraction line at Q = 2.84Å^{-1} appears at T^r = 109°C. Comparing to Pt/Ru = 1.0, it decreased by ~15°C again indicating the reduced activation energy for the growth of Pt shell crystal. In addition, the trend of lattice space with reaction time is similar but in lower extent (from 2.24Å to 2.219Å). This feature explains the strain relaxation at heterogeneous interface by the restructure of Pt into homoatomic domains and the accommodation followed by the propagation of lattice displacement in the shell region with doubled atomic volume[32]. When Pt/Ru = 3.0 (see **Fig. 3b**), the $d_{(111)}$ is determined to be 2.238 Å in the beginning of (111) facet (Q = 2.82Å^{-1}) formation at 109°C and then kept in 2.232Å after T^r > 116°C. The slight decrease of $d_{(111)}$ by less than 0.5% to a stable value suggesting the absence of Ru substrate confinement during the shell crystal growth and the formation of homogeneous PtRu alloy in the shell region. It is important to note the presence of diffraction line of (200) facets at Q = 3.20Å^{-1}) at T^r > 116°C. This character reveals the suppressed preferential shell crystal growth by Pt^{4+} to Ru^0 replacement and the subsequent formation of PtRu alloying comparing to the NCs with Pt/Ru = 1.0 and 2.0.

Taking the above structure evolution into account, the orientation of the shell crystal at Ru core facets can be draw into Scheme 1 by comparing the changes of T_F (T_R) and $d_{(111)}$ with the reaction time. Where, the Ru core is grown in a nano-disk in shape comprising the {0001} face facets and the {1010} radial facets. (a) The growth of shell crystal is preferentially grown at radial facet into {111} with a strong substrate compression strain for Pt/Ru = 1.0 and 2.0 NCs. (c) At the face facets, the shell crystal grown in the opened {0001} facets with suppressed long-range ordering. (b) For Pt/Ru = 3.0 NCs, the severe Pt^{4+} to Ru^0 transmetallation replacement leads to the formation of PtRu alloy in the shell crystal at Ru radial facets. (d) At the face facets, the high density of residual Pt^{4+} results in the certain extent of ordering structure at {200} facets.

CrystEngComm

ARTICLE

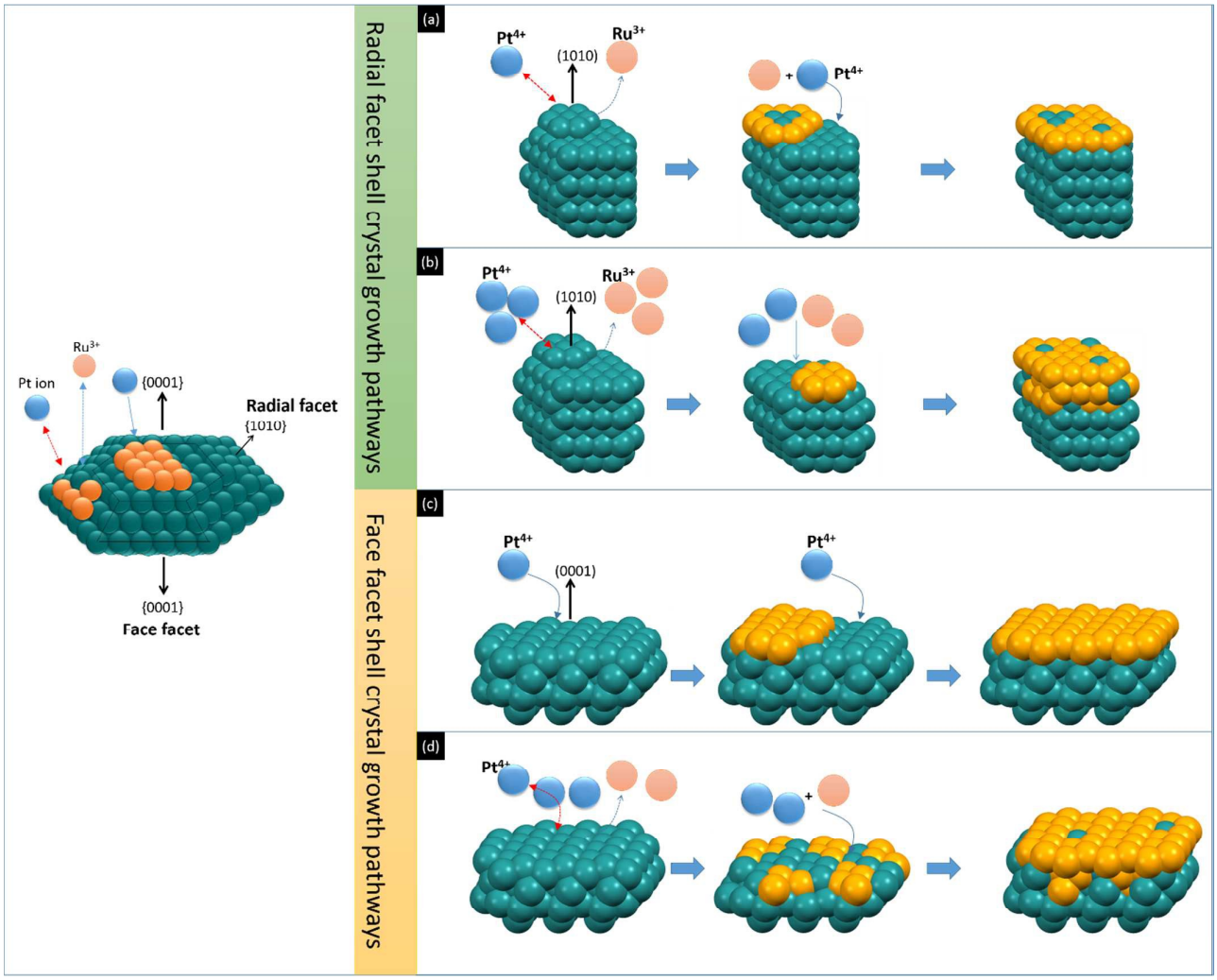

Scheme 1 Heterogeneous nucleation – growth pathways of Pt ions atop radial {1010} facets of (a) Pt/Ru = 1.0, 2.0 NCs, (b) Pt/Ru = 3.0 NCs and face {0001} facets of (c) Pt/Ru = 1.0, 2.0 NCs, (d) Pt/Ru = 3.0 NCs.

Conclusions

We demonstrated the proper strategies on programming the crystal structure of core-shell NCs in expected architectures by combining on the concepts of surface free energy variations of crystal facets and the spontaneous transmetallation replacements. By combining in-situ small angle and wide angle X-ray scattering analysis, we provide the strategies that precisely developed the geometry, the lattice strain, and the composition of the shell crystal via controlling the reagent ratios, the reaction time, and the pre-incubation treatments. According to our results, the growth of the Pt shells on Ru cores follows a heterogeneous nucleation and crystal growth in four-steps: (1) the transmetallation replacement of Pt^{3+} to Ru^{0} in incubation state, (2) the nucleation of Pt nuclei at Ru core surface, (3) the shell crystal growth at radial and face facets of Ru core, and (4) the heteroatomic restructure at shell regions for the case of Pt/Ru < 2.0 NCs. In these regions, the confinement of Ru core facets is strong and resulting in the compression strain progressively increased with the shell crystal growth. For NCs with severe incubation transmetallation (Pt/Ru = 3.0), the shell crystal grown without

the nucleation step of Pt nuclei. In this case, the lattice strain by Ru confinement was merely relaxed therefore resulting in the growth of PtRu alloy in the shell region. Our results show the very first observation on the correlation between lattice strain and the atomic restructure at the shell region by using *in-situ* characterizations. We believed that such real time techniques with model analysis provide the robust and effective strategies for the design of nanocrystallite with expected geometry and configurations that are capable for optimizing the performance of nano-devices in multidisplanary applications.

Acknowledgements

The authors would like to thank the staff of National Synchrotron Radiation Research Center (NSRRC), Hsinchu, Taiwan for the help in various synchrotron-based measurements. T.-Y. Chen acknowledges the funding support from research projects of the National Tsing Hua University, Taiwan (N103K30211 and 103N1200K3) and the Ministry of Science and Technology, Taiwan (MOST 103-2112-M-007 -022 -MY3).

Notes and references

1 R. R. Adzic, J. Zhang, K. Sasaki, M. B. Vukmirovic, M. Shao, J. X. Wang, A. U. Nilekar, M. Mavrikakis, J. A. Valerio and F. Uribe, Topics in Catalysis, 2007, 46, 249-262.
2 K. Sasaki, H. Naohara, Y. Cai, Y. M. Chio, P. Liu, M. B. Vukmirovic, J. X. Wang and R. R. Adzic, Angewandte Chemie International Edition, 2010, 49, 8602-8607.
3 T. Bligaard and J. K. Nørskov, Electrochimica Acta, 2007, 52, 5512-5516.
4 P. Strasser, S. Koh, T. Anniyev, J. Greeley, K. More, C. Yu, Z. Liu, S. Kaya, D. Nordlund, H. Ogasawara, M. F. Toney and A. Nilsson, Nature Chemistry, 2010, 2, 454–460.
5 S. Alayoglu and B. Eichhorn, Journal of the American Chemical Society, 2008, 130, 17479-17486.
6 F. Liu, J. Y. Lee and W. J. Zhou, Small, 2006, 2, 121-128.
7 W. J. Zhou, B. Zhou, W. Z. Li, Z. H. Zhou, S. Q. Song, G. Q. Sun, Q. Xin, S. Douvartzides, M. Goula and P. Tsiakaras, Journal of Power Sources, 2004, 126 16-22.
8 Y.-C. Wei, T.-Y. Chen, C.-W. Liu, T.-S. Chan, J.-F. Lee, C.-H. Lee, L. Tsang-Lang; and K.-W. Wang, Catalysis Science & Technology, 2012.
9 M. Watanabe, M. Uchida and S. Motoo, Journal of Electroanalytical Chemistry, 1987, 229, 395-406.
10 M. P. Hogarth and T. R. Ralph, Platinum Metals Review, 2002, 46, 117-135.
11 Y. Sun and Y. Xia, Advanced Materials, 2002, 14, 833-837.
12 C.-H. Chen, L.-S. Sarma, D.-Y. Wang, F.-J. Lai, C.-C. A. Andra, S.-H. Chang, D.-G. Liu, C.-C. Chen, J.-F. Lee and B.-J. Hwang, ChemCatChem 2010, 2, 159-166.
13 S.-Y. Huang, C. M. Chang, K. W. Wang and C.-T. Yeh, ChemPhysChem, 2007, 8, 1774-1777.
14 14.S. Goto, S. Hosoi, R. Arai, S. Tanaka, M. Umeda, M. Yoshimoto and Y. Kudo, The Journal of Physical Chemistry C, 2014, 118, 2634−2640.
15 T.-Y. Chen, T.-J. M. Luo, Y.-W. Yang, Y.-C. Wei, K.-W. Wang, T.-L. Lin, T.-C. Wen and C.-H. Lee, The Journal of Physical Chemistry C, 2012, 116, 16969−16978.
16 T.-Y. Chen, I.-L. Chen, Y.-T. Liu, T.-L. Lin, P.-W. Yang, C.-Y. Wu, C.-C. Hu, T.-J. M. Luo and C.-H. Lee, CrystEngComm, 2013, 15, 982-994.
17 T.-Y. Chen, T.-L. Lin, T.-J. M. Luo, Y. Chio and J.-F. Lee, ChemPhysChem, 2010, 11, 2383-2392.
18 F.-J. Lai, W.-N. Su, L. S. Sarma, D.-G. Liu, C.-A. Hsieh, J.-F. Lee and B. J. Hwang, Chemistry A European Journal, 2010, 16, 4602-4611.
19 T.-Y. Chen, Y.-T. Liu, H. M. Nguyen, L.-J. Fan, C.-Y. Wu, T.-J. M. Luo, C.-H. Lee, Y.-W. Yang, T.-C. Wen and T.-L. Lin, Journal of Materials Chemistry A, 2013, 1, 5660–5669.
20 C.-Y. Wu, Y.-T. Liu, P.-C. Huang, T.-J. M. Luo, C.-H. Lee, Y.-W. Yang, T.-C. Wen, T.-Y. Chen and T.-L. Lin, Nanoscale 2013, 5, 9181-9192.
21 U.-S. Jeng, C. H. Su, C. J. Su, K.-F. Liao, W.-T. Chuang, Y.-H. Lai, J. W. Chang, Y. J. Chen, Y. S. Huang, M.-T. Lee, K. L. Yu, J. M. Lin, D. G. Liu, C. F. Chang, C. Y. Liu, C. H. Chang and K. S. Liang, J. Appl. Crystallogr., 2010, 43, 110.
22 J.-M. Lin, T.-L. Lin, U.-S. Jeng, Y.-J. Zhong, C.-T. Yeh and T.-Y. Chen, Journal of Applied Crystallography, 2007, 40, s540-s543.
23 J. Teixeira, Journal of Applied Crystallography, 1988, 21, 781-785.
24 S. R. Kline, J. Appl. Cryst. , 2006, 39, 895-900.
25 P. Bartlett and R. H. Ottewill, Journal of Chemical Physics, 1992, 96, 3306.
26 R. S. Justice, D. H. Wang, L.-S. Tan and D. W. Schaefer, J. Appl. Cryst., 2007, 40, s88-s92.
27 V. K. LaMer and R. H. Dinegar, Journal of the American Chemical Society, 1950, 72, 4847-4854.
28 J.-P. Jolivet, Metal Oxide Chemistry and Synthesis - From Solution to Solid State, John Wiley & Sons, Chichester, 2003.
29 S. Alayoglu, A. U. Nilekar, M. Mavrikakis and B. Eichhorn, Nature Materials, 2008, 7, 333-338.
30 T.-Y. Chen, Y.-T. Liu, H.-S. Chen, K.-W. Wang, C.-T. Yang, T.-J. M. Luo, C.-H. Lee and T.-L. Lin, CrystEngComm, 2013, 15, 3932-3942.
31 F. Besenbacher, I. Chorkendorff, B. S. Clausen, B. Hammer, A. M. Molenbroek, J. K. Nørskov and I. Stensgaard, Science, 1998, 279, 1913-1915.
32 A. Schlapka, M. Lischka, A. Gross, U. Kasberger and P. Jakob, Physical Review Letters, 2003, 91, 016101.